Friction **10**(11): 1893–1912 (2022)
https://doi.org/10.1007/s40544-021-0566-5
ISSN 2223-7690
CN 10-1237/TH
RESEARCH ARTICLE

Ionic liquids on uncharged and charged surfaces: *In situ* microstructures and nanofriction

Rong AN[1,*], Yudi WEI[1], Xiuhua QIU[1], Zhongyang DAI[2,*], Muqiu WU[1], Enrico GNECCO[3], Faiz Ullah SHAH[4], Wenling ZHANG[5]

[1] *Herbert Gleiter Institute of Nanoscience, School of Materials Science and Engineering, Nanjing University of Science and Technology, Nanjing 210094, China*

[2] *High Performance Computing Department, National Supercomputing Center in Shenzhen, Shenzhen 518055, China*

[3] *Otto Schott Institute of Materials Research (OSIM), Friedrich Schiller University Jena, Jena 07743, Germany*

[4] *Chemistry of Interfaces, Luleå University of Technology, Luleå 97187, Sweden*

[5] *School of Mechanical Engineering, Nanjing University of Science and Technology, Nanjing 210094, China*

Received: 19 August 2021 / Revised: 27 September 2021 / Accepted: 22 October 2021

Abstract: *In situ* changes in the nanofriction and microstructures of ionic liquids (ILs) on uncharged and charged surfaces have been investigated using colloid probe atomic force microscopy (AFM) and molecular dynamic (MD) simulations. Two representative ILs, [BMIM][BF_4] (BB) and [BMIM][PF_6] (BP), containing a common cation, were selected for this study. The torsional resonance frequency was captured simultaneously when the nanoscale friction force was measured at a specified normal load; and it was regarded as a measure of the contact stiffness, reflecting *in situ* changes in the IL microstructures. A higher nanoscale friction force was observed on uncharged mica and highly oriented pyrolytic graphite (HOPG) surfaces when the normal load increased; additionally, a higher torsional resonance frequency was detected, revealing a higher contact stiffness and a more ordered IL layer. The nanofriction of ILs increased at charged HOPG surfaces as the bias voltage varied from 0 to 8 V or from 0 to −8 V. The simultaneously recorded torsional resonance frequency in the ILs increased with the positive or negative bias voltage, implying a stiffer IL layer and possibly more ordered ILs under these conditions. MD simulation reveals that the $[BMIM]^+$ imidazolium ring lies parallel to the uncharged surfaces preferentially, resulting in a compact and ordered IL layer. This parallel "sleeping" structure is more pronounced with the surface charging of either sign, indicating more ordered ILs, thereby substantiating the AFM-detected stiffer IL layering on the charged surfaces. Our *in situ* observations of the changes in nanofriction and microstructures near the uncharged and charged surfaces may facilitate the development of IL-based applications, such as lubrication and electrochemical energy storage devices, including supercapacitors and batteries.

Keywords: microstructure; friction; contact stiffness; charged surfaces; ionic liquids (ILs); molecular simulation

1 Introduction

Ionic liquids (ILs) are liquid molten organic salts composed of cations and anions with melting points of < 100 °C. ILs have garnered substantial research interests owing to their exceptional properties, such as low vapor pressure, non-flammability, excellent thermal conductivity, high ionic conductivity, high chemical and thermal stabilities, and wide electrochemical stability windows [1–3]. These properties render ILs extremely promising for a range of electrochemical and engineering applications, e.g.,

* Corresponding authors: Rong AN, E-mail: ran@njust.edu.cn; Zhongyang DAI, E-mail: daizy@nsccsz.cn

energy storage and lubrication [4–9]. It is noteworthy that the adsorption/moving dynamics and microstructures of ILs adjacent to surfaces are vital to electrochemical reactions occurring at electrode surfaces, as well as to the effective boundary lubrication of sliding contact surfaces [4, 10]. For instance, it was observed that the ionic conductivity of confined ILs in silica nanoparticles decreased compared with that in the bulk, which was likely due to the low ion mobility in the nanoconfined ILs [11]. A smaller diffusion coefficient was recorded for an IL confined between graphite walls compared with that in the bulk [12]. However, both experimentalists and theorists discovered the acceleration of ion diffusion in confined systems [13–16]. For example, the diffusion coefficient of ions in phosphonium bis(salicylato)borate IL confined in 4 nm Vycor pores is discovered to be 35–40 times greater than that in the bulk [15].

The dynamics of ions in ILs on charged interfaces is more complicated than that on uncharged surfaces. Rajput et al. [17] observed that the diffusion of ions in an IL confined inside a slit graphitic nanopore with a width of 5.2 nm was greater at charged walls compared with neutral ones. A more recent study by Wu et al. [18] indicated an opposite trend, i.e., ions at charged surfaces propagated slower than those at neutral ones, and the ions propagated slower as the charge density increased.

It was reported that the frictionless surface of confined walls exhibited a strong correlation with the liquid diffusion acceleration and reduction [19–21]. We previously employed nanofriction measured via atomic force microscopy (AFM) to describe the mobility of supported polymer films [22]. Recently, "nanofriction" has been considered as a good indicator of interfacial ion mobility for describing the dynamics of ILs at interfaces [13, 23]. This is because nanofriction is sensitive to variations in the microstructures of ILs at sliding surfaces, e.g., the interfacial IL ordering [24–26]. Increased nanofriction is discovered in confined ILs as the number of ion layers decreased [25, 27, 28]. The higher number of ordered IL layers with a greater concentration of excess ions closer to the confined surfaces contributed to the increased nanofriction [25]. However, a different effect of the ordered IL layers on the nanofriction was also reported in Refs. [24, 28, 29], in which well-formed interfacial structures of ILs facilitated the formation of a lubricating sliding plane, resulting in enhanced lubricity and lower nanofriction. This clearly contradicts the effect of IL microstructures on the nanofriction at IL–solid interfaces.

The microstructures of ILs can be manipulated by charging the confined surfaces to create an electric field across the nanoscale IL film [30, 31]. Both experimental and theoretical findings indicate that nanoconfined charged surfaces enable IL ordering into alternating charge layers [25, 32–34]. In particular, the microstructural changes of near-surface ILs, i.e., liquid-to-solid phase shifts, were discovered to be induced by surface charging [35], which was more pronounced for metallic surfaces [36]. In addition, ordered solid-phase ILs resulting from surface charging are expected to decrease nanoscale friction by preventing direct surface-to-surface contact [36]. We previously combined AFM measurements with molecular dynamics (MD) simulations to unravel the microscopic mechanisms that determined the nanofriction response in terms of IL microstructures [13]. In this study, it was discovered via simulation that changes in the nanofriction and microstructure occurred simultaneously at IL–solid interfaces and were associated with each other [13]. However, *in situ* nanofriction–microstructure changes of near-surface ILs have not been observed experimentally, particularly when the surfaces are charged.

In this study, colloid probe AFM was employed to elucidate *in situ* nanofriction–microstructure changes of ILs on uncharged and charged surfaces. SiO_2 (silica) and polymethyl methacrylate (PMMA) colloid probes were used instead of standard sharp tips. The tribo-interface in IL systems scanned via AFM can be regarded as a complex "black box" (the left panel in Scheme 1(a)) composed of an AFM probe, ILs, and solid surfaces with characteristic roughness, chemical heterogeneities, charges, etc. Two questions arise: How can one consider the contribution of solid surfaces, and how can one detect the simultaneous nanofriction–microstructure changes of ILs occurring at IL–solid interfaces? Hence, in this study, we utilized colloid probes to model solid surfaces (the right panel in Scheme 1(a)) to directly detect nanofriction at the IL–solid interface. The torsional resonance frequency

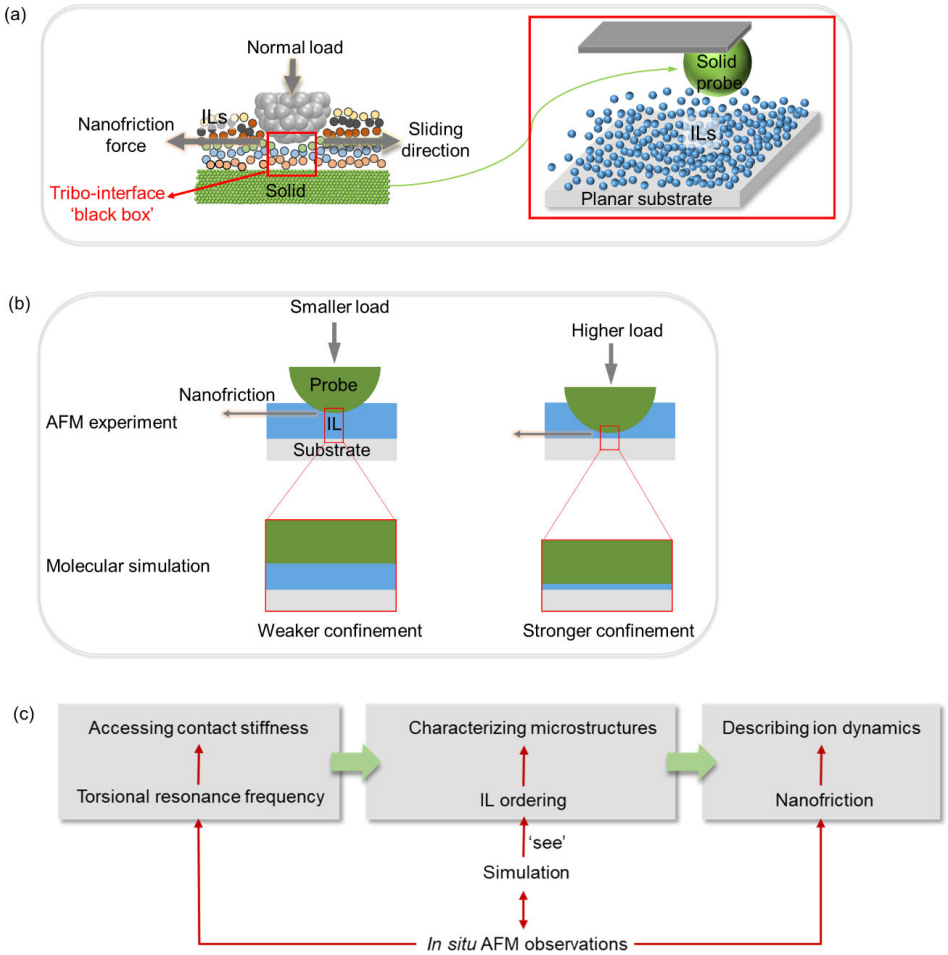

Scheme 1 Schematic illustrations of (a) simplified IL–solid model with two ILs, i.e., BB and BP, for investigating *in situ* nanofrictional and microstructural changes at IL–solid interfaces; (b) confinement in molecular simulation corresponding to AFM-measured nanofriction; and (c) the general overview of interdependencies among nanofriction, microstructure, IL ordering, and ion dynamics.

is captured simultaneously when the nanoscale friction force is measured at a specified normal load. This frequency is an indicator of the contact stiffness [37, 38], which reflects *in situ* IL microstructural changes. A higher contact stiffness is indicative of more ordered IL layers, as confirmed by our simulation. The two extensively investigated ILs, 1-butyl-3-methylimidazolium tetrafluoroborate, ([BMIM][BF_4], BB) and 1-butyl-3-methylimidazolium hexafluorophosphate, ([BMIM][PF_6], BP), serve as well-defined model systems for investigating *in situ* changes in the nanofriction and microstructure of ILs on uncharged and charged surfaces.

We employed bare SiO_2 and PMMA probes to simplify the solid surfaces that were in contact with the ILs and simultaneously captured the nanofriction and torsional resonance frequency at the IL–solid interfaces. The nanofriction obtained is a good indicator of the interfacial ion mobility for describing the dynamics of ILs at interfaces and it is vital to electrochemical reactions and boundary lubrication. It is noteworthy that the colloid probe propagates closer to the substrate when the applied normal load increases, thereby resulting in varying confinements for the ILs (the top panel in Scheme 1(b)). Hence, a slit–pore model was used in the MD simulation to mimic the colloid probe approaching uncharged and charged surfaces (the bottom panel in Scheme 1(b)) to investigate the IL ordering at interfaces as well as to confirm the experimentally detected microstructural changes (Scheme 1(c)). A general overview of the interdependencies among nanofriction, confinement, microstructure, IL ordering, and ion dynamics is shown in Schemes 1(b) and 1(c).

2 Experimental and simulation

2.1 Preparation of AFM colloid probes

Dodecenyl succinic anhydride (DDSA) and benzyldimenthylamine (BDMA) were purchased from Sinopharm Chemical Reagent Co., Ltd., China and Araldite Resin CY212 (CY212) was obtained from Sigma-Aldrich, USA. Rectangular AFM PNP-DB cantilevers were purchased from Nanoworld, Switzerland. SiO_2 (silica) and PMMA microspheres (20 μm in dimension) were obtained from EPRUI Biotech Co., Ltd., USA, The AFM colloid probes were prepared by attaching SiO_2 microspheres to rectangular cantilevers (type: PNP-DB, and the cantilever 1 with a nominal spring constant of 0.48 N/m was used) with epoxy glue (BDMA:DDSA:CY212 = 1:10:10 in volume ratio). The surface morphologies of the AFM colloid probes were observed using the scanning electron microscope (SEM; JSM-IT500HR, JEOL, Japan) and AFM. Silica and PMMA colloid probes were glued using a double-sided tape on a mica support, which had been placed onto a steel disc to enable magnetic fixation under the scanning tip in tapping mode with a 240AC-NA cantilever (tip radius < 7 nm, OPUS, Mikromasch Europe, Germany). The focused scanning positions of these colloid probes were monitored using the optical microscope equipped in the AFM system prior to imaging.

2.2 Preparation of IL films on mica and highly oriented pyrolytic graphite (HOPG) surfaces

Mica and HOPG were purchased from Electron Microscopy Sciences, USA and MikroMasch, USA, respectively. ILs, 1-butyl-3-methylimidazolium tetrafluoroborate (BB, purity ≥ 98%) and 1-butyl-3-methylimidazolium hexafluorophosphate (BP, purity ≥ 97%), were purchased from Sigma-Aldrich, USA. To prepare films on the surfaces of mica and HOPG, the ILs were dissolved in ethanol to yield IL solutions with a concentration of 10^{-3} mL IL in 1 mL ethanol. The as-prepared IL solutions (1 μL) were deposited either on mica or HOPG substrates (area = 1 cm × 1 cm); subsequently, the ethanol was allowed to completely evaporate in vacuum at 35 °C for 12 h to obtain IL films. The morphologies of BB and BP on the mica and HOPG surfaces were scanned in our previous study [27] via tapping mode AFM using silicon probes, as shown in Fig. S1 in the Electronic Supplementary Material (ESM). Extended layering structures were clearly observed, and some of the IL drops resided on the layering-assembled IL films, forming drop-on-layer structures.

2.3 *In situ* friction force and torsional resonance frequency measurements

The friction force measurements were performed on a Dimension Icon AFM (Bruker, Germany) in contact mode under ambient conditions. The as-prepared SiO_2 and PMMA colloid probes were employed throughout the friction measurements with a scan rate of 2 Hz under the probe at a 90° scan angle to the cantilever long axis. The lateral calibration of cantilevers supporting the colloid probes was performed based on the method of Liu et al. [39]. The *in situ* changing torsional resonance frequency was simultaneously recorded by capturing the lateral friction force and it is a useful indicator of the probe-IL contact stiffness. The torsional resonance frequency measurements were conducted by performing a frequency sweep with "high speed data capture" in the Dimension Icon AFM to obtain the amplitude spectra (lateral deflection vs. frequency). Surface charging was performed by applying biased sample voltages (−8 to 8 V) to the HOPG-supported ILs on the AFM sample holder, where the probe was connected to the ground.

SiO_2 and PMMA colloid probes were utilized to measure the net adhesion forces of the ILs using the probes based on a continuous approach via AFM. The adhesion forces reported in terms of cantilever deflection vs. the separation distance could be acquired as the force jump during retraction, which represented the pull-off force required to separate the probe after contact.

2.4 MD simulation

The slit model was used to investigate the molecular properties of fluids under confinement [40–42]. In our typical AFM experiments, SiO_2 microspheres and HOPG were used as the AFM probe and substrate with ILs between them. Hence, we constructed a slit pore model with a SiO_2 slab as the probe and a three-layer graphene sheet as the substrate in the

simulation. The ILs, i.e., BB and BP, were confined in the SiO_2–graphene slit pore (Fig. 1). The SiO_2 slab and graphene sheets were arranged parallel to the *X*–*Y* plane and fixed as such with a dimension of 6.20 nm × 6.24 nm, thereby allowing the flow of sufficient ILs to obtain reliable statistical results. Slit pores with varying pore widths of 1, 2, 5, and 10 nm were utilized to mimic the probe approaching the surface at different normal loads [43, 44], in which the probe was placed closer to the surface to accommodate a relatively high normal load. We applied the voltages of 8 and −8 V on the ILs confined in a 2 nm SiO_2–graphene slit pore along the *Z*-axis using the constant potential method to determine the effect of surface voltages on the IL microstructures. At the voltages of 8 and −8 V, the electric field was directed toward SiO_2 and graphene, respectively. The number of confined ion pairs (Table S1 in the ESM) was calculated using an effective volume based on the bulk density of the ILs [45, 46] in the slit pore, which provided an accurate estimate of the density of the confined ILs. For example, we placed 119, 238, 597, and 1,194 ion pairs of BB inside the modeling systems with slit pore widths of 1, 2, 5, and 10 nm, respectively (Table S1 in the ESM). A three-dimensional (3D) periodic boundary condition was applied to the simulation box. Periodic boundary conditions were applied in all directions, and a 5 nm vacuum gap was set on the top plane of the SiO_2 slab and the bottom plane of the graphene sheets to eliminate image effects in the *Z*-axis direction.

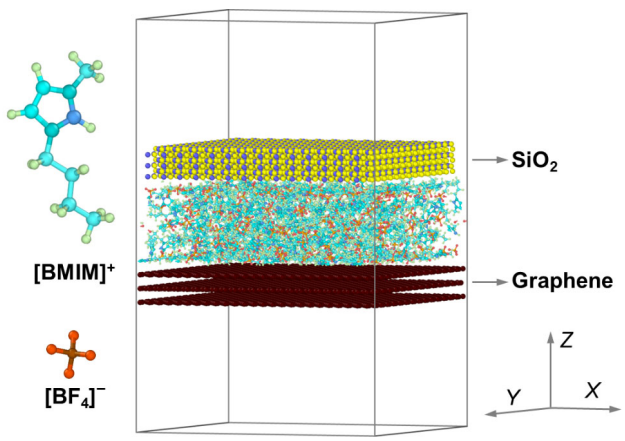

Fig. 1 Molecular configuration of cation $[BMIM]^+$ and anion $[BF_4]^-$ of BB, and image of BB confined in a 2 nm graphene–SiO_2 slit pore. Detailed molecular structures of BB and BP are illustrated in Table S2 in the ESM.

The refined force field of imidazolium-based ILs developed by Liu et al. [47] was employed to describe BB and BP in our study. This model was modified based on the assisted model building with energy refinement force field and had been proven suitable for simulating the microstructures of ILs at solid interfaces, which was consistent with experimental results [47, 48]. It was noteworthy that the Hertzian contact pressure in the graphite system with the SiO_2 probe was estimated to be 5–15 MPa at varying normal loads in the AFM measurements, whereas this pressure was 11–63 MPa at different confinements in the MD simulation. Because the order of magnitude of the pressure during the AFM experiments agreed well with that in the MD simulation, it was inferred that the force field parameters used in our systems were reasonable and acceptable. The force-field parameters for SiO_2 were extracted from Ref. [49], whereas those for HOPG were obtained from Ref. [50]. In the present study, we constructed SiO_2 slit pores without considering the surface chemistry, such as the surface hydroxylation of SiO_2, as in Ref. [51]. The Lennnard–Jones 12–6 and Coulombic potential models were used to determine the van der Waals (vdW) and electrostatic interactions, and the relevant parameters are listed in Table S2 in the ESM. The Lorentz–Berthelot combining rules were used to determine the vdW interactions for different types of atoms. All equilibrated simulation systems were simulated in an *NVT* ensemble at 300 K using the Nose–Hoover thermostat with a damping time of 100.0 fs. Noting that an ensemble with three parameters (the number of particles *N*, the volume *V*, and the absolute temperature *T*) is called the *NVT* ensemble. The motion of atoms was described using the classical Newton equation, which was solved using the velocity-Verlet algorithm with a 1.0 fs time step. The cutoff distance of the vdW and electronic interactions was 1.2 nm, and the particle–particle particle–mesh method was employed to calculate long-range electrostatic interactions [52, 53]. All MD simulations were performed using the large-scale atomic/molecular massively parallel simulator package [54]. The simulation system was relaxed and optimized for 20 ns to obtain an equilibrium state, and the trajectory coordinates of the molecules were obtained within 20 ns, with a storage frequency of 100 time steps.

3 Results and discussion

3.1 Morphology of AFM colloid probes

SiO_2 and PMMA microspheres with a diameter of ~20 μm were attached at the end of the rectangular cantilevers, as shown in Figs. 2(a) and 2(b), respectively. Enlarged AFM images show the local surface features of the obtained SiO_2 and PMMA colloid probes. A slight difference is observed between the roughness of the SiO_2 and PMMA colloid probes, with the surface of the SiO_2 probe (R_q = 34.6±1.7 nm; R_q is the root-mean-squared roughness.) being slightly smoother than that of PMMA (R_q = 38.4±1.5 nm).

The nanoscale roughness significantly affects the friction force and the roughness effects depending on the contact stress [55]. In an earlier study, it was discovered that the friction coefficient increased monotonically with the roughness of the contacts mediated by the IL ethylammonium nitrate using AFM colloid probes [56]. Furthermore, MD simulations show that friction at contacts lubricated by the ILs can either increase [57] or decrease [58] with the surface roughness. The measured roughness presented in Fig. 2 shows that the SiO_2 and PMMA colloid probes possess similar surface roughnesses; therefore, any significant differences caused by this parameter are negligible.

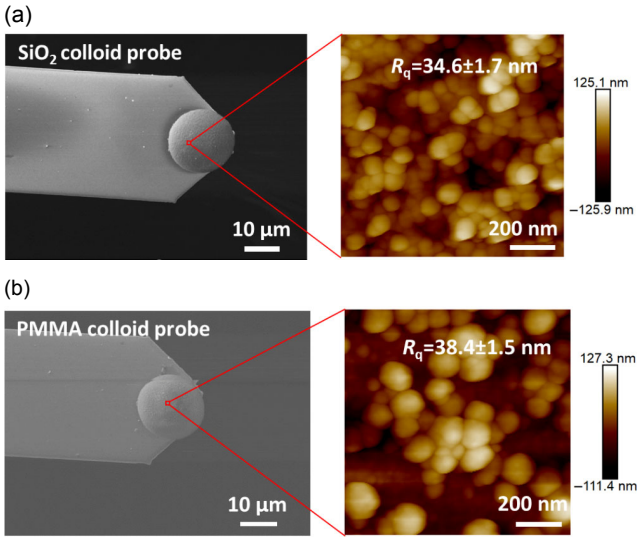

Fig. 2 SEM (left) and AFM topographic (right) images of (a) SiO_2 and (b) PMMA colloid probes.

3.2 *In situ* nanofriction–microstructure changes of ILs on uncharged surfaces

3.2.1 *Nanofriction of ILs on uncharged surfaces*

The friction force (F_F) of ILs BB and BP on the uncharged mica and HOPG surfaces as functions of normal load (F_N) are shown in Figs. 3(a) and 3(b), respectively, using the SiO_2 and PMMA colloid probes. The average friction coefficient μ (*cf.* Table 1) is determined from the gradient of F_F vs. F_N based on the modified Amontons' law of friction, $F_F = \mu F_N + F_0$, where F_0 is the friction force at zero applied normal load. The nonzero intercept, F_0, depends on the lubricant between the sliding surfaces, as well as the roughness and compressibility of the probe/sample [56, 59, 60].

Greater friction forces are observed in the ILs on mica (Fig. 3(a)) compared with those on HOPG (Fig. 3(b) and Fig. S2 in the ESM) for both the SiO_2 and PMMA probes. This may be because the surface of mica is negatively charged owing to the presence of K^+ [61], whereas the HOPG surface is neutral. Previously, we performed X-ray photoelectron spectroscopy (XPS) to confirm that the imidazolium ring in BB or BP interacted vigorously with the surface of mica via a covalent bond formed between the N atom of the ring and the Si atom of mica [27]. For ILs on HOPG surfaces, Yokota et al. [62] and Sha et al. [63] speculated the preferential interaction of the imidazolium ring in the cation $[BMIM]^+$ with the surface of graphene. Furthermore, it was discovered that the tilt angle of the plane of the ring with respect to the surface normal significantly affected the friction, in which a smoother and better-defined shear plane facilitated friction reduction [64].

As shown in Table 1, the friction coefficient μ measured for BP supported by mica with a SiO_2 colloid probe is 0.23±0.021, whereas that for BB is higher ($\bar{\mu}$ = 0.40±0.017). By contrast, as shown in Fig. 3(b) and Table 1, the friction force and the resulting friction coefficient are greater ($\bar{\mu}$ = 0.064±0.003) in the HOPG-supported BP than those in BB ($\bar{\mu}$ = 0.010±0.001). Furthermore, the friction force F_F was affected by the probe material, in which the values of F_F for a specified IL were higher when PMMA colloid probes were used instead of SiO_2 (Fig. 3(a)). The resulting friction coefficients $\bar{\mu}$ on the mica surface obtained using PMMA colloid probes are 0.32±0.012 and

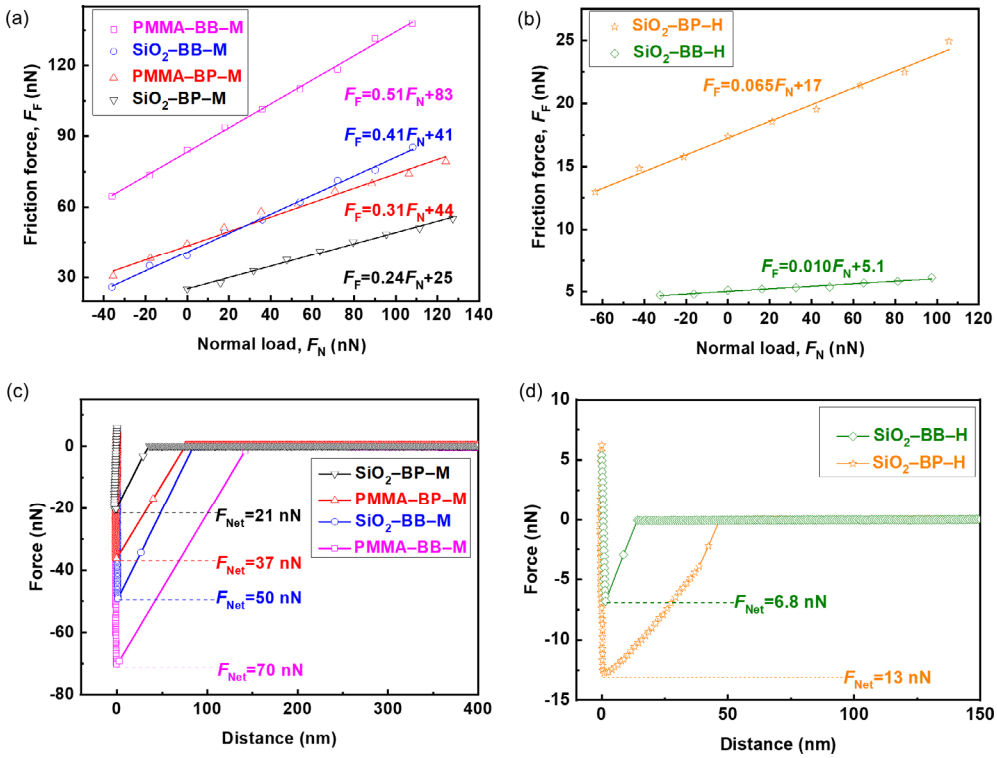

Fig. 3 Representative friction force (F_F) vs. normal load (F_N) curves for SiO_2 and PMMA AFM colloid probes sliding over ILs (BB and BP) films on (a) mica and (b) HOPG substrates. Fitting slope represents friction coefficient μ, based on Amontons' law of friction. Representative retracting force vs. distance curves of SiO_2 and PMMA colloid probes with ILs BB and BP on (c) mica and (d) HOPG substrates for obtaining their net adhesion forces, F_{Net}. SiO_2–BP–M represents a SiO_2 colloid probe sliding over the BP film formed on the mica surface. The definitions of the abbreviations are provided in Table 1.

Table 1 Nanoscale average friction coefficients of SiO_2 and PMMA AFM colloid probes sliding over BB and BP films on mica and HOPG surfaces, and average net adhesion forces of colloid probes with ILs on mica and HOPG surfaces.

Probe–IL–substrate	Average friction coefficient, $\bar{\mu}$	Average net adhesion force, $\bar{F}_{Net}$ (nN)
SiO_2–BP–M[a]	0.23±0.021[d]	21±1.80
SiO_2–BB–M	0.40±0.017	51±0.87
PMMA–BP–M[b]	0.32±0.012	36±1.30
PMMA–BB–M	0.53±0.021	71±1.30
SiO_2–BP–H[c]	0.064±0.003	13±1.30
SiO_2–BB–H	0.010±0.001	6.8±0.82

[a]SiO_2 colloid probe sliding over BP film formed on mica surface (M); [b]PMMA colloid probe sliding over BP film formed on mica surface; [c]SiO_2 colloid probe sliding over BP film formed on HOPG surface (H); [d]Error values of obtained friction coefficient and net adhesion forces corresponding to standard deviation of mean.

0.53±0.021 for BP and BB, respectively, which are higher than those obtained using SiO_2 (0.23±0.021 and 0.40±0.017 for BP and BB, respectively) (Table 1).

3.2.2 *Adhesion forces*

The observed higher friction is contributed primarily by the greater probe–IL interactive strength [65] and enhanced IL ordering [25]. Our previous findings combining AFM measurements and the corresponding state theory reveal that stronger liquid–solid interactions result in a higher friction coefficient at the liquid–solid interface [65]. To substantiate this, we captured the first force–distance curve for the colloid probe at the BB or BP surface supported by mica and HOPG to quantitatively examine the interactive force of the colloid probe toward the IL (Figs. 3(c) and 3(d)). The obtained net adhesion force ($\bar{F}_{Net}$) provided a direct measure of the probe–IL interactive strength. We discovered that the $\bar{F}_{Net}$ ranked in the following order (Table 1): PMMA–BB–M ($\bar{F}_{Net}$ = 71±1.30 nN) > SiO_2–BB–M ($\bar{F}_{Net}$ = 51±0.87 nN) > PMMA–BP–M ($\bar{F}_{Net}$ = 36±1.30 nN) > SiO_2–BP–M ($\bar{F}_{Net}$ = 21±1.80 nN) > SiO_2–BP–H ($\bar{F}_{Net}$ = 13±1.30 nN) > SiO_2–BB–H ($\bar{F}_{Net}$ = 6.8±0.82 nN). Hence, it is conceivable that a stronger

friction is measured by the PMMA probe on the ILs as compared with the SiO_2 probe. The different adhesion forces obtained are primarily caused by vdW, electrostatic, and capillary meniscus forces, which are significantly associated with the surface properties of the probe and substrate, as well as the ILs between them [66–68].

It is noteworthy that when the same colloid probe was used on the mica substrates, the measured probe–IL interaction, F_{Net}, was significantly higher in BB than that in BP, which resulted in stronger friction in BB. By contrast, on the HOPG substrates, F_{Net} was higher in BP than that in BB when the same colloid probe was used, demonstrating stronger friction in BP. It is noteworthy that a sharp break occurred in the detachment of the SiO_2 probe from the BB on the HOPG surface, whereas a gradual response was observed from BP. This indicates that BP is pulled away by the SiO_2 probe during detachment owing to the enhanced electrostatic interactions of BP with the SiO_2 probe, stemming from the higher electron densities in $[PF_6]^-$ anions [69] compared with those in $[BF_4]^-$. The gradual detachment behavior is not observed in the colloid probes with ILs on the mica surface, which is likely due to the stronger interactions between the ILs and the mica substrate [27].

3.2.3 *Contact stiffness*

The contact stiffness can be indirectly assessed [70] from the torsional resonance frequency, which can be simultaneously measured with the friction force [37, 38] indicative of the IL ordering at interfaces. The higher contact stiffness associated with enhanced IL ordering contributes partially to the higher friction. Smith et al. [25], An et al. [27], and Cooper et al. [28] discovered that more ordered ILs resulted in a higher friction force. This might be because IL ordering resulted in a greater concentration of excess ions, thus resulting in a stronger "interlayer attraction for the same contact area" [25]. As shown in Fig. 4, the torsional resonance frequency is higher in a specified IL when the PMMA colloid probe is used instead of SiO_2, reflecting a higher contact stiffness at the PMMA–IL interface. By using the same colloid probe, the torsional resonance frequency was discovered to be higher at the mica-supported BB surface than that at the BP surface.

3.2.4 *Substrate effect on in situ nanofriction–microstructure changes of ILs on uncharged surfaces*

To further investigate the contribution of the substrate to the *in situ* nanofriction–microstructure changes of ILs on uncharged surfaces, we investigated HOPG-supported IL systems using SiO_2 colloid probes (Fig. 5). As the normal load increased, i.e., the probe penetrated through an additional ion layer closer to the substrate [44] (*cf.* Scheme 1(b)), the position of the torsional resonance peak on the HOPG-supported ILs shifted to a higher frequency, indicating a higher contact stiffness. The contact stiffnesses and friction forces at the SiO_2–BP interfaces (Fig. 5(a)) are higher than those at the SiO_2–BB interfaces (Fig. 5(b)) under a similar range of applied normal loads. Compared with the mica-supported BB system shown in Fig. 4(b), the contact stiffnesses obtained on the HOPG-supported BB surfaces using SiO_2 colloid probes are lower and hence indicate smaller friction forces (Fig. 5(b)). It is noteworthy that the colloid probes and the substrates are not in direct contact during the friction measurements, as confirmed by the higher contact stiffness on the IL-coated substrates as compared with the bare substrates (Figs. 4 and 5 and Fig. S3 in the ESM).

3.3 *In situ* nanofriction–microstructure changes in ILs on charged surfaces

It was previously reported that the effect of surface charging on the IL microstructures at interfaces resulted in a considerable variation in the nanofriction forces owing to the surface charging density [71]. However, the correlation between charge-dependent nanofriction and near-surface IL microstructures, i.e., *in situ* nanofriction–microstructure changes in ILs on charged surfaces, is yet to be elucidated. Using the HOPG-supported ILs (BB and BP) system as an example, the nanofriction and torsional resonance spectra were measured simultaneously using SiO_2 colloid probes under varying negative and positive bias voltages (Fig. 6).

It is discovered that nanofriction indicates a monotonic dependence on the surface charges [72], although not for all cases [32, 71]. In our case, we observed that the nanofriction of BB and BP on the charged HOPG surfaces increased as the positive-bias voltage increased

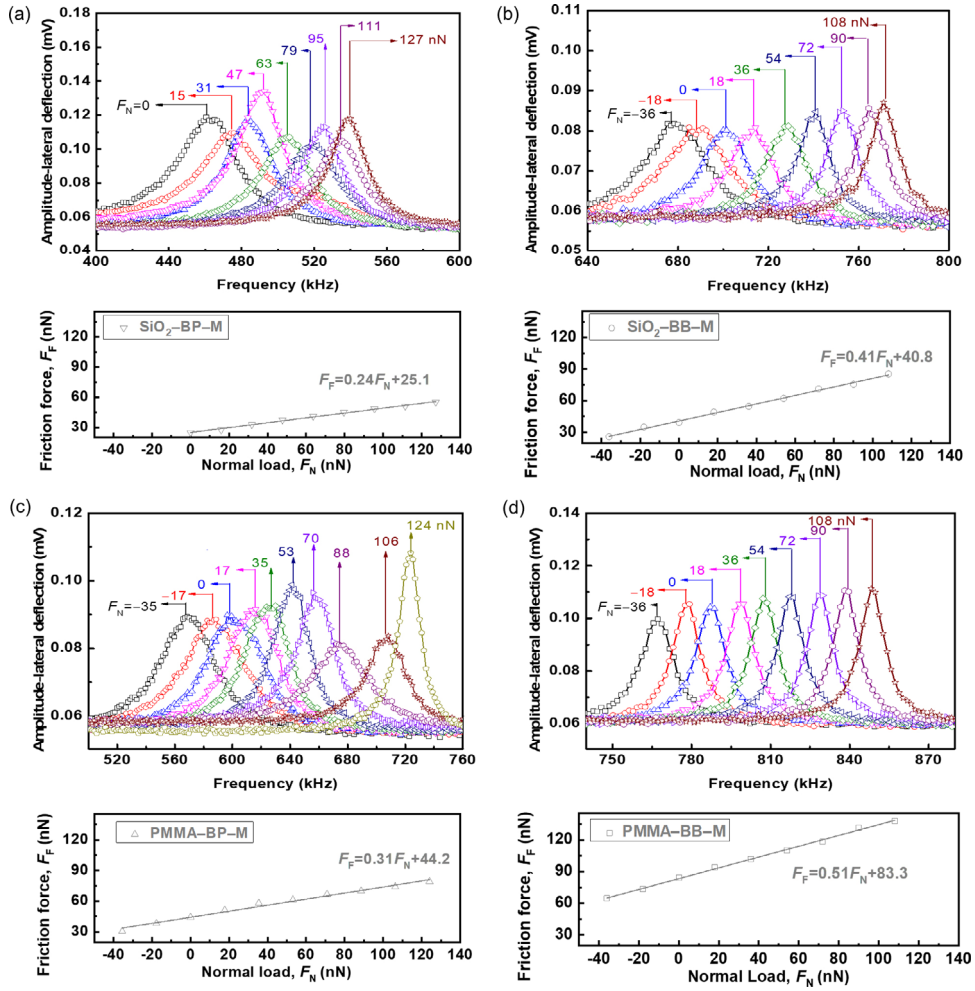

Fig. 4 In (a) SiO_2–BP–M, (b) SiO_2–BB–M, (c) PMMA–BP–M, and (d) PMMA–BB–M systems: (a–d, top) torsional resonance spectra from lateral/friction force signal (simultaneously recorded with friction force) measured using SiO_2 and PMMA colloid probes at BP and BB surfaces supported by mica under varying normal loads, respectively; (a–d, bottom) *in situ* changes in friction force vs. normal load (from Fig. 3).

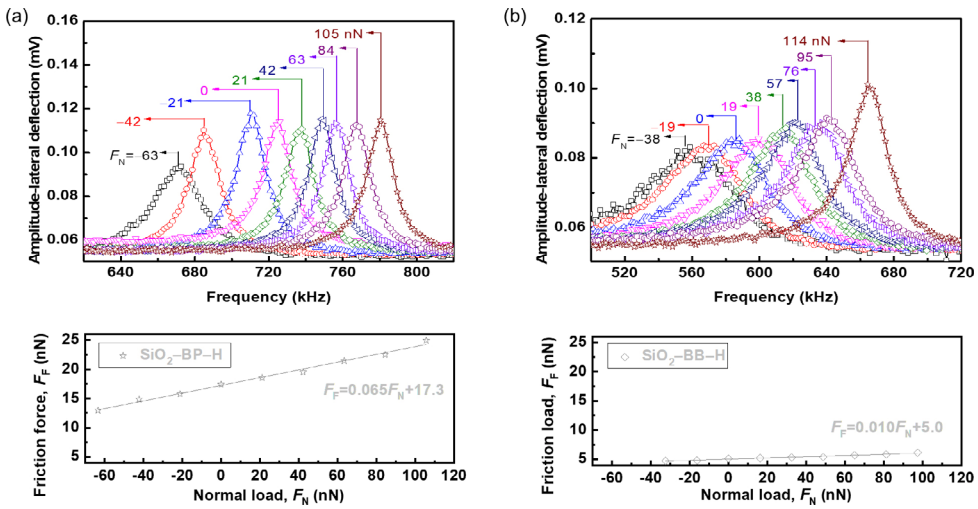

Fig. 5 In (a) SiO_2–BP–H and (b) SiO_2–BB–H systems, top: torsional resonance spectra from lateral/friction force signal (simultaneously recorded with friction force) measured using SiO_2 colloid probe at BP and BB surfaces supported by HOPG under varying normal loads, respectively; bottom: *in situ* changes in friction force vs. normal load (from Fig. 3).

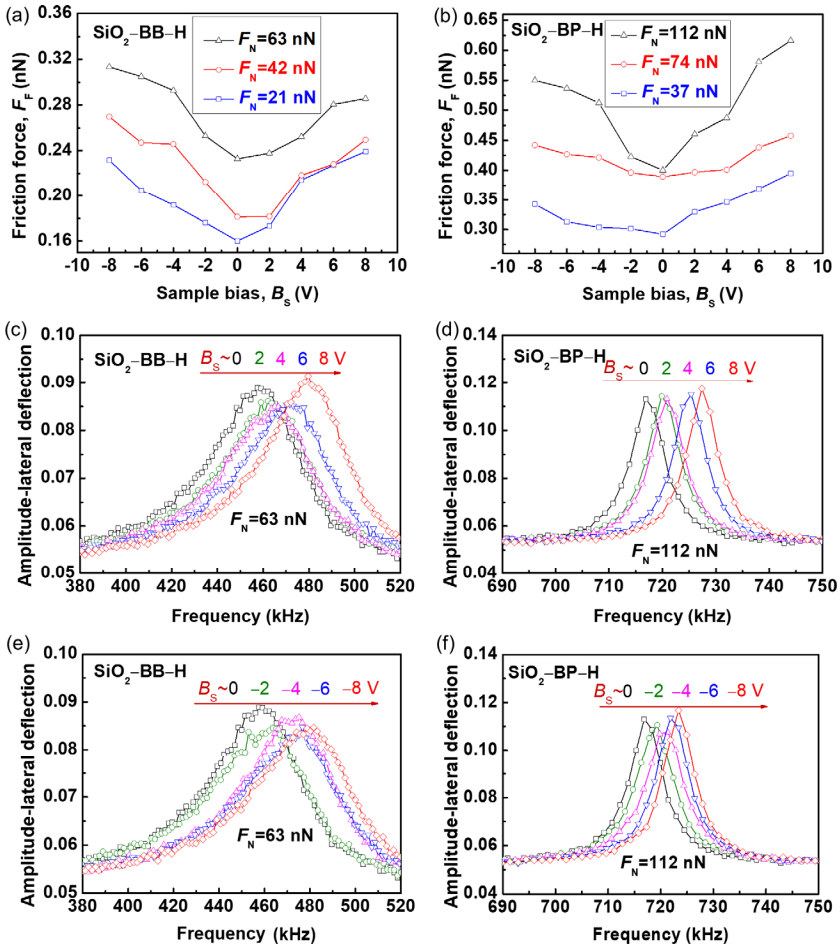

Fig. 6 Friction force as a function of sample bias (B_S) measured on (a) BB and (b) BP at HOPG surfaces using SiO_2 colloid probes at various normal loads. (c–f) *In situ* changes in torsional resonance spectra recorded with friction force obtained in (a) and (b) under different sample biases, at normal load of 63 nN for SiO_2–BB–H with (c) positive-bias and (e) negative-bias voltages, and 112 nN for SiO_2–BP–H with (d) positive-bias and (f) negative-bias voltages. *In situ* changes in torsional resonance spectra recorded at other normal loads are shown in Fig. S4 in the ESM.

from 0 to 8 V (Figs. 6(a) and 6(b)). A similar variation tendency was discovered under negative-bias voltages from 0 to −8 V, although the friction forces under positive-bias voltages were smaller than those under negative-bias voltages at the same voltage values. A similar behavior was observed for the changes in the friction force with the sample bias at various applied normal loads (F_N = 21, 42, and 63 nN for BB; 37, 74, and 112 nN for BP).

At a specified normal load (e.g., F_N = 63 nN), the simultaneously recorded torsional resonance frequencies in the BB increase as the positive- or negative-bias voltages increase (458 → 480 kHz when 0 → 8 V (Fig. 6(c)), and 458 → 481 kHz when 0 → −8 V (Fig. 6(e))). This phenomenon is less evident in the BP at a normal load of 112 nN (717 → 727 kHz when 0 → 8 V (Fig. 6(d)) and 717 → 723 kHz when 0 → −8 V (Fig. 6(f))). The torsional resonance frequencies at other normal loads for both BB and BP exhibit the increasing trend when a higher sample bias is applied (Fig. S4 in the ESM). This implies there is a higher contact stiffness when a higher sample bias (B_S) is applied, corresponding to more ordered ILs at the interfaces, which also contributes to the simultaneously observed higher friction force [25].

3.4 Microstructures of ILs on uncharged surfaces at atomic scale

3.4.1 *Ion orientation evaluated using orientational order parameter*

To obtain more insights into the changes in contact

stiffness on uncharged and charged surfaces, the variation in the orientational order parameter (denoted as S) as the SiO_2 probe approached the ion layers at graphite surfaces was investigated further via MD simulations. The orientational order parameter S is defined as the ensemble average of the second Legendre polynomial, which is expressed as [73, 74]:

$$S = \frac{3\cos^2\theta - 1}{2} \quad (1)$$

where θ is the angle between the imidazolium ring normal of the cation $[BMIM]^+$ and the surface normal (Z-axis). The values of S vary from −0.5 to 1, and $S = -0.5$ indicates that the imidazolium ring normal is perpendicular to the surface normal (θ = 90°); meanwhile, $S = 1$ indicates that they are parallel to each other (θ = 0° or 180°), corresponding to the two typical orientation structures of the imidazolium ring (structures (I) and (II)) in Fig. 7(a). In the disordered isotropic bulk phase of the IL, S equals 0. The orientational order parameter S offers a clear depiction of the orientational preference of $[BMIM]^+$ in the X–Y plane.

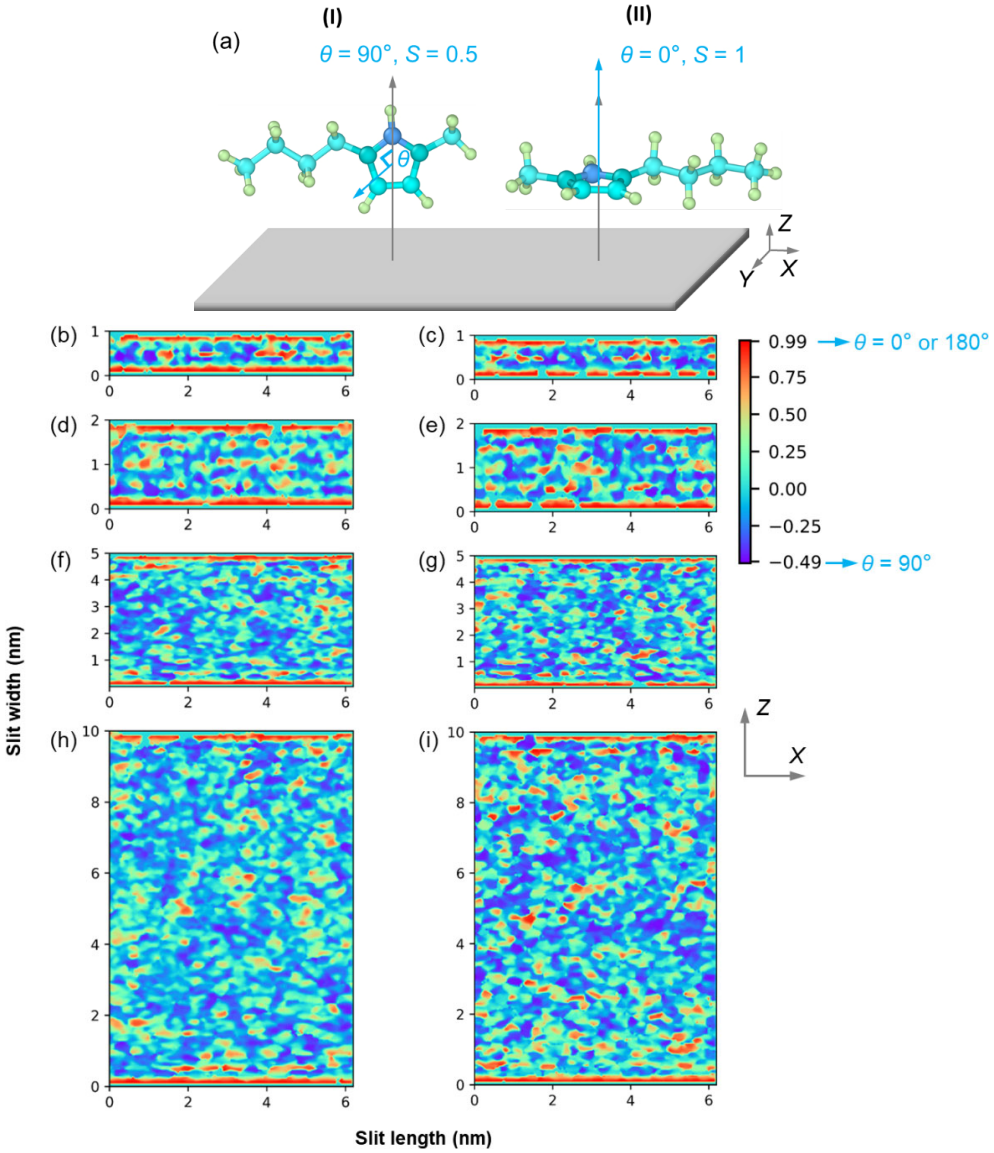

Fig. 7 (a) Two typical orientation structures of imidazolium ring: (I) θ = 90° and (II) θ = 0°. Contour plots of imidazolium ring distribution (described via orientational order parameter S) of (b, d, f, h) BB and (c, e, g, i) BP confined in uncharged graphene–SiO_2 slit pores with width ranging from 1 to 10 nm: (b, c) 1 nm, (d, e) 2 nm, (f, g) 5 nm, and (h, i) 10 nm. Bottom of slit pores is three-layer graphene (slit width = 0 nm), and the top is SiO_2 surface. The values of S (vertical scale) change from −0.5 to 1.

In the AFM experiments, the colloid probe approached the substrate as the applied normal load increased. Hence, a slit-pore model was employed to mimic the probe approaching the substrate by varying the confinement widths (1, 2, 5, and 10 nm), in which a smaller width corresponded to a higher normal load. The slit pore was composed of a SiO_2 probe and a three-layered graphene substrate. The number density profiles suggest that the ions of ILs prefer to accumulate at the surface of the slit pores to form a compact and ordered structure, independent of the slit width (Fig. S5 in the ESM).

The two-dimensional (2D) contour plots of the imidazolium ring distribution of BB and BP confined in the graphene–SiO_2 slit pores are further illustrated in Figs. 7(b)–7(i), which show different preferential orientations of the imidazolium ring to the surface of the X–Y plane. The blue and red regions indicate that the imidazolium ring normal is perpendicular (structure (I)) and parallel (structure (II)) to the surface normal, respectively, whereas the green region corresponds to irregular orientations, i.e., the disordered isotropic bulk phase. As shown in Figs. 7(b)–7(i), the imidazolium ring normal vector is parallel to the surface normal in all slit widths (1, 2, 5, and 10 nm), indicating that the imidazolium ring is "sleeping" in parallel onto the surface of the slit pore (red, structure II, θ = 0° or 180°). This parallel "sleeping" structure results in the accumulation of ions at the surface of the slit pores, thereby facilitating the formation of more compact and ordered ion layers. The other dominant structure (blue, structure (I), θ = 90°) appears discontinuous within the slit pore, implying that this structure is less favorable for the formation of compact and ordered ion layers. It is clear that the orientational ordering of both BB and BP is more pronounced as the slit widths decrease from 10 to 1 nm. This confirms the higher degree of ordering within the ion layer at a higher normal load and a higher contact stiffness, as shown in Fig. 5.

3.4.2 *Angular probability distributions*

To further investigate the ion distribution on the surface, the detailed angular probability distributions for the imidazolium ring, butyl chains, and anions on the HOPG and SiO_2 surfaces without biased voltages are presented in Fig. 8 and Fig. S6 in the ESM. On the HOPG surface (Fig. 8(a) and Fig. S6(a) in the ESM), for both BB and BP, most of the imidazolium rings lie almost flat along the surface ($\theta \approx 7°$ or 170°) for all slit pore widths (1, 2, 5, and 10 nm) because of the π–π interactions between the cations and the graphene

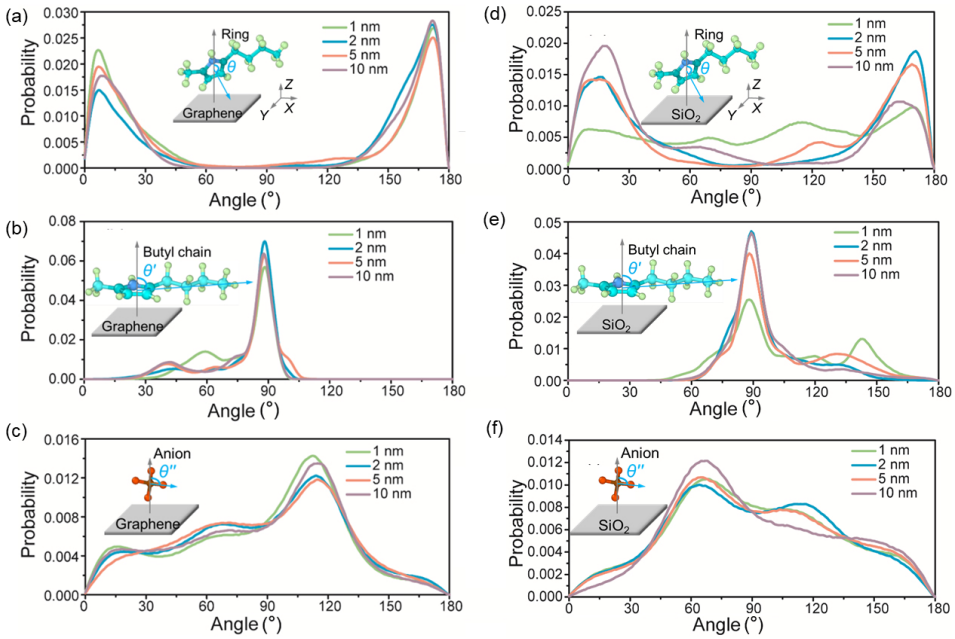

Fig. 8 Angular probability distributions for imidazolium ring of cation $[BMIM]^+$, butyl chain, and anion $[BF_4]^-$ of BB on the surfaces of (a, b, c) graphene and (d, e, f) SiO_2 under confinement. The insets show typical configurations of the (a), (d) imidazolium ring; (b), (e) butyl chain; and (c), (f) anion on the surfaces.

surface [75]. A parallel orientation of the butyl chains along the graphene surface was observed in both BB (Fig. 8(b)) and BP (Fig. S6(b) in the ESM). The $[BF_4]^-$ anions show a tilted orientation of approximately 118° from the HOPG surface normal (Fig. 8(c)), whereas the angle probability distribution between the $[PF_6]^-$ anion and HOPG surface normal exhibits two pronounced peaks at approximately 53° and 125° (Fig. S6(b) in the ESM). Typical configurations of the butyl chain and anion on surfaces are shown in the insets of Figs. 8(b)–8(f) and Figs. S6(b)–S6(f) in the ESM.

Unlike the almost perfectly parallel orientation of the imidazolium ring plane on the HOPG surface, the $[BMIM]^+$ cations of both BB (Fig. 8(d)) and BP (Fig. S6(d) in the ESM) exhibit preferential distributions for maximizing hydrogen bonding interactions between the cations and the dangling O atoms on the SiO_2 surface [69, 75, 76]. We observed that angles θ of approximately 15° and 170° were favored by the imidazolium ring distance from the SiO_2 surface but with a broad rough angle probability distribution in between, indicating different distributions for the configurations and orientations of the cations on SiO_2 from those on the graphene surface. The broad rough peaks in the imidazolium ring probability distribution profiles indicate that a few rings exhibit tilted orientations from the SiO_2 surface in varying slit pores. The observed angles of 90° in the butyl chains of both BB and BP to the surface normal correspond to the chains "sleeping" on the SiO_2 surface (Fig. 8(e) and Fig. S6(e) in the ESM). In contrast to the HOPG surface, the majority of $[BF_4]^-$ anions exhibit a tilted orientation of approximately 65° from the SiO_2 surface, and some of them are tilted 90°–150° away from the surface (Fig. 8(f)). The $[PF_6]^-$ anions indicate maximum values at approximately 53° and 125° on the SiO_2 surface, which is less probable on the HOPG surface, corresponding to the weaker adsorption of this conformation on SiO_2 (Fig. S6(f) in the ESM).

3.5 Surface charging on microstructures of ILs

3.5.1 Ion orientation and number density profiles

The effect of charging on the orientation of $[BMIM]^+$ cations confined in 2 nm graphene–SiO_2 slit pores is shown in Fig. 9(a). The parallel orientation of the imidazolium ring (red, structure (II), $\theta = 0°$ or 180°) dominates at the uncharged surfaces of the slit pore, thereby facilitating the formation of compact and ordered ion layers. In comparison, the parallel "sleeping" structure (II) is more pronounced during the slit pore charging of either sign (8 V, −8 V) in both BB (the left panel in Fig. 9(a)) and BP (the right panel in Fig. 9(a)). This implies more ordered ions at the charged surfaces, which agreed well with the stiffer AFM-detected ion layers at the surfaces with either positive- or negative-bias voltages, as shown in Fig. 6. Except for the $[BMIM]^+$ cation, the $[BF_4]^-$ and/or $[PF_6]^-$ anions dominated the layer composition, as shown in the number density profiles (Fig. 9(b)), and primarily adhered to the vicinity of the slit pore surface. The number density profiles in Fig. 9(b) show well-defined interfacial structures of ions at the charged slit pores (width = 2 nm) under biased voltages of 8 and −8 V. The cations accumulate near the graphene surface at −8 V, whereas more anions accumulate near the SiO_2 surface. By contrast, at a biased voltage of 8 V, cations and anions accumulate near the SiO_2 and graphene surfaces, respectively. This indicates the ordering of ILs into alternating charge layers at the charged surfaces. The compact and ordered IL layers formed on the charged surfaces result in a greater friction force [25] than those on the uncharged surfaces. In comparison with the ion accumulation at 0 V, the accumulation of ions near the charged graphene and SiO_2 surfaces under biased voltages of 8 and −8 V is not distinct, which is likely due to the steric hindrance that the slit pore can exert on the internal IL structure [77].

3.5.2 Angular probability distributions

It is noteworthy that the differences in the contour plots of the imidazolium ring distribution under biased voltages can not be observed clearly with the naked eye. Hence, we provide detailed angular probability distributions of the imidazolium ring, butyl chains, and anions on HOPG and SiO_2 surfaces (slit width = 2 nm) under biased voltages of 8 and −8 V, as shown in Fig. 10 and Fig. S7 in the ESM, which show different accumulations of cations and anions.

As shown in Fig. 10(a) and Fig. S7(a) in the ESM, on the HOPG surface at 8 V, the angles between the imidazolium ring are normal for BB and BP, as well as the surface normal are 8°–25° and 160°–170°,

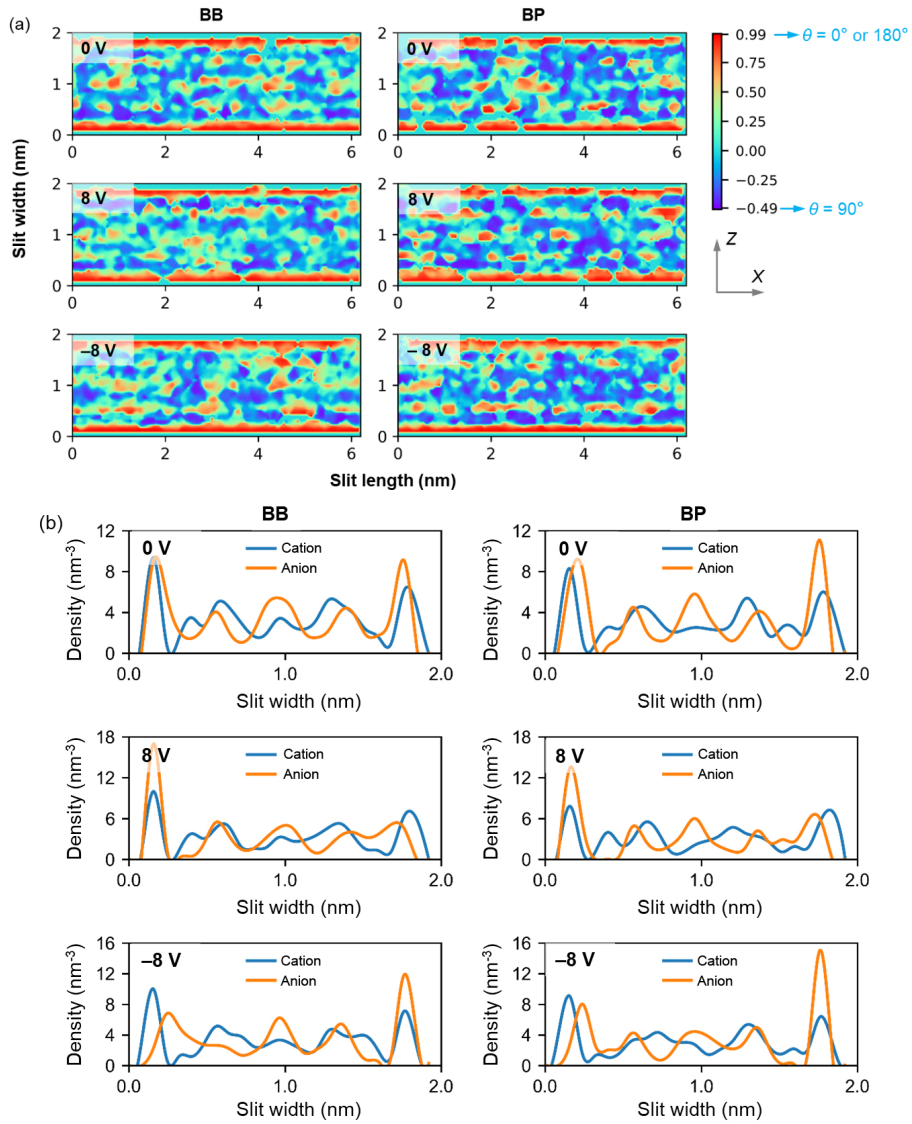

Fig. 9 (a) Contour plots of imidazolium ring distribution (described via orientational order parameter *S*) of BB (left panel) and BP (right panel) confined in a 2 nm graphene–SiO_2 slit pore with applied voltages of 0, 8, and −8 V. The bottom of slit pore is three-layer graphene (slit width = 0 nm), and the top is SiO_2 surface. (b) Number density profiles of cation and anion of BB (left panel) and BP (right panel) confined in a 2 nm graphene–SiO_2 slit pore with applied voltages of 0, 8, and −8 V. Slit width = 0 nm represents three-layer graphene, and slit width = 2 nm represents SiO_2 surface.

respectively, without distinct peaks in between. This indicates that most of the imidazolium rings are almost parallel to the surface. Under an applied voltage of −8 V, the angular probability distributions of the imidazolium ring for BB and BP exhibit two pronounced sharp distribution peaks at approximately 8° and 170°. The butyl chains of both BB and BP are oriented approximately 90° from the HOPG surface normal under either 8 or −8 V, as shown in Fig. 10(b) and Fig. S7(b) in the ESM. Figure 10(c) shows that the $[BF_4]^-$ anions are tilted 14° and 110° from the surface normal at 8 V, whereas they are tilted 65° from the surface with a broad distribution at 90°–170° under −8 V. Meanwhile, the $[PF_6]^-$ anion exhibits two pronounced peaks at approximately 53° and 125° at both 8 and −8 V, as shown in Fig. S7(c) in the ESM.

On the SiO_2 surface, the orientational angles of the imidazolium rings for the BB (Fig. 10(d)) show two peaks at approximately 14° and 170° at 8 V, whereas those at −8 V show two peaks at approximately 23° and 160°. For BP, as shown in Fig. S7(d) in the ESM, the imidazolium rings tilt by 10° and 170° from the

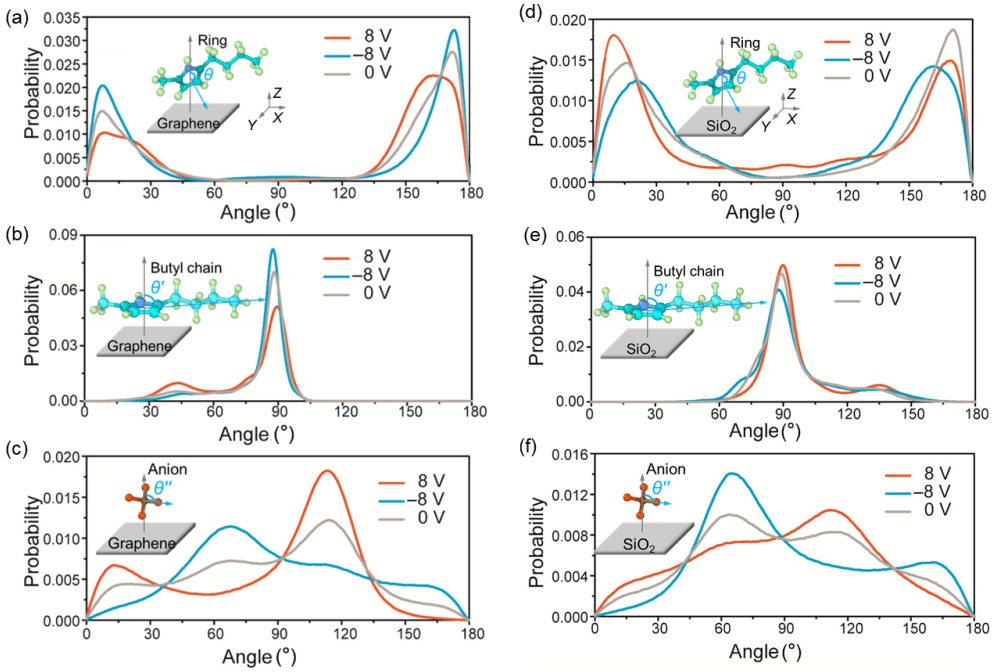

Fig. 10 Angular probability distributions for the imidazolium ring of cation $[BMIM]^+$, butyl chain, and anion $[BF_4]^-$ of BB on (a, b, c) graphene and (d, e, f) SiO_2, when IL is confined in a 2 nm slit pore with applied voltages of 0, −8, and 8 V.

SiO_2 surface at 8 V; however, a broad-blunt angular probability distribution is observed as well. By contrast, at −8 V, the imidazolium rings of BP tilt more toward the SiO_2 surface with tilt angles of 18° and 155°. The butyl chains of BB (Fig. 10(e)) and BP (Fig. S7(e) in the ESM) tilt approximately 90° from the SiO_2 surface normal under either 8 or −8 V. Figure 10(f) shows that the anion $[BF_4]^-$ is oriented 115° from the SiO_2 surface normal at 8 V, and 63° under −8 V. Compared with the anion $[PF_6]^-$ of BP shown in Fig. S7(f) in the ESM, it tilts by approximately 53° and 125° from the surface normal under −8 V; however, two broad and weak peaks at 60° and 122° are observed in $[PF_6]^-$ at 8 V (Fig. S7(f) in the ESM).

4 Conclusions

Colloid probe AFM was employed to investigate *in situ* changes in the nanofriction and microstructures of ILs (BB and BP) on uncharged and charged surfaces. A higher nanoscale friction force and a higher torsional resonance frequency were observed when the normal load on the uncharged surfaces increased. A higher torsional resonance frequency at a higher normal load corresponded to a higher contact stiffness, indicating a more compact and ordered IL layer that provided a higher friction. By contrast, on the charged surfaces, the nanofriction of the ILs increased with the positive-bias voltage, and a similar variation tendency was observed under the negative-bias voltages. The dependence of friction force on the applied bias voltage was similar at various normal loads. Additionally, the recorded torsional resonance frequency in the ILs was higher when a higher surface bias of either sign was applied, indicating a stiffer, more compact, and ordered IL layer, which contributed to the higher friction on the charged surfaces. MD simulations showed that the parallel orientation of the imidazolium ring in the $[BMIM]^+$ cation dominated on the uncharged surfaces of the adopted slit pore model, thereby facilitating the formation of compact and ordered ion layers. Additionally, the parallel "sleeping" structure was more pronounced on the charged surfaces, which implied more ordered ions; this confirmed the presence of stiffer ion layers, as detected via AFM on the charged surfaces. These findings are expected to contribute significantly to the use of ILs as lubricants in electric vehicles, electrolytes in energy storage devices, and other applications where charged surfaces are used.

Acknowledgements

This work was supported by the Natural Science Foundation of Jiangsu Province (No. BK20191289), the National Natural Science Foundation of China (Nos. 21838004, 21978134, and 21676137), the National Key R&D Program of China (No. 2018YFB0204403), the Swedish Research Council (No. 2018-04133), and the German Research Foundation, DFG (No. GN 92/16-1). The permission of the figure reproduction in Fig. S1 in the ESM is acknowledged.

Electronic Supplementary Material Supplementary material is available in the online version of this article at https://doi.org/10.1007/s40544-021-0566-5.

References

[1] Zhou Y, Qu J. Ionic liquids as lubricant additives: A review. *ACS Appl Mater Interfaces* **9**(4): 3209–3222 (2017)

[2] Lhermerout R, Perkin S. Nanoconfined ionic liquids: Disentangling electrostatic and viscous forces. *Phys Rev Fluids* **3**(1): 014201 (2018)

[3] Wang Y L, Wang C L, Zhang Y Q, Huo F, He H Y, Zhang S J. Molecular insights into the regulatable interfacial property and flow behavior of confined ionic liquids in graphene nanochannels. *Small* **15**(29): e1804508 (2019)

[4] Cai M R, Yu Q L, Liu W M, Zhou F. Ionic liquid lubricants: When chemistry meets tribology. *Chem Soc Rev* **49**(21): 7753–7818 (2020)

[5] Wang Y L, Li B, Sarman S, Mocci F, Lu Z Y, Yuan J Y, Laaksonen A, Fayer M D. Microstructural and dynamical heterogeneities in ionic liquids. *Chem Rev* **120**(13): 5798–5877 (2020)

[6] Bi S, Banda H, Chen M, Niu L, Chen M Y, Wu T Z, Wang J S, Wang R X, Feng J M, Chen T Y, et al. Molecular understanding of charge storage and charging dynamics in supercapacitors with MOF electrodes and ionic liquid electrolytes. *Nat Mater* **19**(5): 552–558 (2020)

[7] Mao X W, Brown P, Červinka C, Hazell G, Li H, Ren Y Y, Chen D, Atkin R, Eastoe J, Grillo I, et al. Self-assembled nanostructures in ionic liquids facilitate charge storage at electrified interfaces. *Nat Mater* **18**(12): 1350–1357 (2019)

[8] Rakov D A, Chen F F, Ferdousi S A, Li H, Pathirana T, Simonov A N, Howlett P C, Atkin R, Forsyth M. Engineering high-energy-density sodium battery anodes for improved cycling with superconcentrated ionic-liquid electrolytes. *Nat Mater* **19**(10): 1096–1101 (2020)

[9] Zhou F, Liang Y M, Liu W M. Ionic liquid lubricants: Designed chemistry for engineering applications. *Chem Soc Rev* **38**(9): 2590–2599 (2009)

[10] Gil P S, Jorgenson S J, Riet A R, Lacks D J. Relationships between molecular structure, interfacial structure, and dynamics of ionic liquids near neutral and charged surfaces. *J Phys Chem C* **122**(48): 27462–27468 (2018)

[11] Unemoto A, Iwai Y, Mitani S, Baek S W, Ito S, Tomai T, Kawamura J, Honma I. Electrical conductivity and dynamics of quasi-solidified lithium-ion conducting ionic liquid at oxide particle surfaces. *Solid State Ion* **201**(1): 11–20 (2011)

[12] Sha M L, Wu G Z, Liu Y S, Tang Z F, Fang H P. Drastic phase transition in ionic liquid [Dmim][Cl] confined between graphite walls: New phase formation. *J Phys Chem C* **113**(11): 4618–4622 (2009)

[13] An R, Zhou G, Zhu Y, Zhu W, Huang L, Shah F U. Friction of ionic liquid–glycol ether mixtures at titanium interfaces: Negative load dependence. *Adv Mater Interfaces* **5**(14): 1800263 (2018)

[14] Filippov A, Antzutkin O N. Magnetic field effects dynamics of ethylammonium nitrate ionic liquid confined between glass plates. *Phys Chem Chem Phys* **20**(9): 6316–6320 (2018)

[15] Filippov A, Azancheev N, Shah F U, Glavatskih S, Antzutkin O N. Self-diffusion of phosphonium Bis(Salicylato)Borate ionic liquid in pores of Vycor porous glass. *Microporous Mesoporous Mater* **230**: 128–134 (2016)

[16] Pinilla C, Del Pópolo M G, Lynden-Bell R M, Kohanoff J. Structure and dynamics of a confined ionic liquid. Topics of relevance to dye-sensitized solar cells. *J Phys Chem B* **109**(38): 17922–17927 (2005)

[17] Rajput N N, Monk J, Hung F R. Structure and dynamics of an ionic liquid confined inside a charged slit graphitic

nanopore. *J Phys Chem C* **116**(27): 14504–14513 (2012)

[18] Wu B N, Breen J P, Xing X Y, Fayer M D. Controlling the dynamics of ionic liquid thin films via multilayer surface functionalization. *J Am Chem Soc* **142**(20): 9482–9492 (2020)

[19] Bocquet L. Nanofluidics coming of age. *Nat Mater* **19**(3): 254–256 (2020)

[20] Majumder M, Chopra N, Andrews R, Hinds B J. Enhanced flow in carbon nanotubes. *Nature* **438**(7064): 44 (2005)

[21] Secchi E, Marbach S, Niguès A, Stein D, Siria A, Bocquet L. Massive radius-dependent flow slippage in carbon nanotubes. *Nature* **537**(7619): 210–213 (2016)

[22] An R, Huang L, Mineart K P, Dong Y, Spontak R J, Gubbins K E. Adhesion and friction in polymer films on solid substrates: Conformal sites analysis and corresponding surface measurements. *Soft Matter* **13**(19): 3492–3505 (2017)

[23] Fan P, Qiu X, Shah F U, Ji Q, An R. The effect of nanoscale friction of mesoporous carbon supported ionic liquids on the mass transfer of CO_2 adsorption. *Phys Chem Chem Phys* **22**(3): 1097–1106 (2020)

[24] Li H, Rutland M W, Atkin R. Ionic liquid lubrication: Influence of ion structure, surface potential and sliding velocity. *Phys Chem Chem Phys* **15**(35): 14616–14623 (2013)

[25] Smith A M, Lovelock K R J, Gosvami N N, Welton T, Perkin S. Quantized friction across ionic liquid thin films. *Phys Chem Chem Phys* **15**(37): 15317–15320 (2013)

[26] Di Lecce S, Kornyshev A A, Urbakh M, Bresme F. Electrotunable lubrication with ionic liquids: The effects of cation chain length and substrate polarity. *ACS Appl Mater Interfaces* **12**(3): 4105–4113 (2020)

[27] An R, Qiu X H, Shah F U, Riehemann K, Fuchs H. Controlling the nanoscale friction by layered ionic liquid films. *Phys Chem Chem Phys* **22**(26): 14941–14952 (2020)

[28] Cooper P K, Wear C J, Li H, Atkin R. Ionic liquid lubrication of stainless steel: Friction is inversely correlated with interfacial liquid nanostructure. *ACS Sustain Chem Eng* **5**(12): 11737–11743 (2017)

[29] Li H, Rutland M W, Watanabe M, Atkin R. Boundary layer friction of solvate ionic liquids as a function of potential. *Faraday Discuss* **199**: 311–322 (2017)

[30] Fedorov M V, Kornyshev A A. Ionic liquids at electrified interfaces. *Chem Rev* **114**(5): 2978–3036 (2014)

[31] Fajardo O Y, Bresme F, Kornyshev A A, Urbakh M. Electrotunable friction with ionic liquid lubricants: How important is the molecular structure of the ions? *J Phys Chem Lett* **6**(20): 3998–4004 (2015)

[32] Fajardo O Y, Bresme F, Kornyshev A A, Urbakh M. Electrotunable lubricity with ionic liquid nanoscale films. *Sci Rep* **5**: 7698 (2015)

[33] Capozza R, Benassi A, Vanossi A, Tosatti E. Electrical charging effects on the sliding friction of a model nano-confined ionic liquid. *J Chem Phys* **143**(14): 144703 (2015)

[34] Smith A M, Parkes M A, Perkin S. Molecular friction mechanisms across nanofilms of a bilayer-forming ionic liquid. *J Phys Chem Lett* **5**(22): 4032–4037 (2014)

[35] Ntim S, Sulpizi M. Role of image charges in ionic liquid confined between metallic interfaces. *Phys Chem Chem Phys* **22**(19): 10786–10791 (2020)

[36] Comtet J, Niguès A, Kaiser V, Coasne B, Bocquet L, Siria A. Nanoscale capillary freezing of ionic liquids confined between metallic interfaces and the role of electronic screening. *Nat Mater* **16**(6): 634–639 (2017)

[37] Rabe U, Amelio S, Kester E, Scherer V, Hirsekorn S, Arnold W. Quantitative determination of contact stiffness using atomic force acoustic microscopy. *Ultrasonics* **38**(1–8): 430–437 (2000)

[38] Maier S, Sang Y, Filleter T, Grant M, Bennewitz R, Gnecco E, Meyer E. Fluctuations and jump dynamics in atomic friction experiments. *Phys Rev B* **72**(24): 245418 (2005)

[39] Liu W H, Bonin K, Guthold M. Easy and direct method for calibrating atomic force microscopy lateral force measurements. *Rev Sci Instrum* **78**(6): 063707 (2007)

[40] Ruiz-Barragan S, Muñoz-Santiburcio D, Marx D. Nanoconfined water within graphene slit pores adopts distinct confinement-dependent regimes. *J Phys Chem Lett* **10**(3): 329–334 (2019)

[41] Qiu Y H, Chen Y F. Capacitance performance of sub-2 nm graphene nanochannels in aqueous electrolyte. *J Phys Chem C* **119**(42): 23813–23819 (2015)

[42] Feng G, Cummings P T. Supercapacitor capacitance exhibits oscillatory behavior as a function of nanopore size. *J Phys Chem Lett* **2**(22): 2859–2864 (2011)

[43] Vilhena J G, Pimentel C, Pedraz P, Luo F, Serena P A, Pina C M, Gnecco E, Pérez R. Atomic-scale sliding friction on graphene in water. *ACS Nano* **10**(4): 4288–4293 (2016)

[44] Black J M, Zhu M Y, Zhang P F, Unocic R R, Guo D Q, Okatan M B, Dai S, Cummings P T, Kalinin S V, Feng G, et al. Fundamental aspects of electric double layer force-distance measurements at liquid–solid interfaces using atomic force microscopy. *Sci Rep* **6**: 32389 (2016)

[45] Dai Z, Shi L, Lu L, Sun Y, Lu X. Unique structures and vibrational spectra of protic ionic liquids confined in TiO_2 slits: The role of interfacial hydrogen bonds. *Langmuir* **34**(44): 13449–13458 (2018)

[46] Singh R, Monk J, Hung F R. A computational study of the behavior of the ionic liquid $[BMIM^+][PF_6^-]$ confined inside multiwalled carbon nanotubes. *J Phys Chem C* **114**(36): 15478–15485 (2010)

[47] Liu Z P, Huang S P, Wang W C. A refined force field for molecular simulation of imidazolium-based ionic liquids. *J Phys Chem B* **108**(34): 12978–12989 (2004)

[48] Dommert F, Schmidt J, Qiao B, Zhao Y, Krekeler C, Delle Site L, Berger R, Holm C. A comparative study of two classical force fields on statics and dynamics of [EMIM][BF_4] investigated via molecular dynamics simulations. *J Chem Phys* **129**(22): 224501 (2008)

[49] Kumar K, Kumar A. Enhanced CO_2 adsorption and separation in ionic-liquid-impregnated mesoporous silica MCM-41: A molecular simulation study. *J Phys Chem C* **122**(15): 8216–8227 (2018)

[50] Shao Q, Zhou J, Lu L, Lu X, Zhu Y, Jiang S. Anomalous hydration shell order of Na^+ and K^+ inside carbon nanotubes. *Nano Lett* **9**(3): 989–994 (2009)

[51] Shi W, Luebke D R. Enhanced gas absorption in the ionic liquid 1-n-hexyl-3-methylimidazolium bis(trifluoromethyl-sulfonyl)amide ([hmim][Tf_2N]) confined in silica slit pores: A molecular simulation study. *Langmuir* **29**(18): 5563–5572 (2013)

[52] Yang D S, Fu F J, Li L, Yang Z, Wan Z, Luo Y, Hu N, Chen X S, Zeng G X. Unique orientations and rotational dynamics of a 1-butyl-3-methyl-imidazolium hexafluoro-phosphate ionic liquid at the gas–liquid interface: The effects of the hydrogen bond and hydrophobic interactions. *Phys Chem Chem Phys* **20**(17): 12043–12052 (2018)

[53] Willcox J A L, Kim H, Kim H J. A molecular dynamics study of the ionic liquid, choline acetate. *Phys Chem Chem Phys* **18**(22): 14850–14858 (2016)

[54] Plimpton S. Fast parallel algorithms for short-range molecular dynamics. *J Comput Phys* **117**(1): 1–19 (1995)

[55] Nalam P C, Sheehan A, Han M W, Espinosa-Marzal R M. Effects of nanoscale roughness on the lubricious behavior of an ionic liquid. *Adv Mater Interfaces* **7**(17): 2000314 (2020)

[56] Asencio R Á, Cranston E D, Atkin R, Rutland M W. Ionic liquid nanotribology: Stiction suppression and surface induced shear thinning. *Langmuir* **28**(26): 9967–9976 (2012)

[57] David A, Fajardo O Y, Kornyshev A A, Urbakh M, Bresme F. Electrotunable lubricity with ionic liquids: The influence of nanoscale roughness. *Faraday Discuss* **199**: 279–297 (2017)

[58] Mendonça A C F, Pádua A A H, Malfreyt P. Nonequilibrium molecular simulations of new ionic lubricants at metallic surfaces: Prediction of the friction. *J Chem Theory Comput* **9**(3): 1600–1610 (2013)

[59] Li H, Somers A E, Howlett P C, Rutland M W, Forsyth M, Atkin R. Addition of low concentrations of an ionic liquid to a base oil reduces friction over multiple length scales: A combined nano- and macrotribology investigation. *Phys Chem Chem Phys* **18**(9): 6541–6547 (2016)

[60] Feiler A A, Stiernstedt J, Theander K, Jenkins P, Rutland M W. Effect of capillary condensation on friction force and adhesion. *Langmuir* **23**(2): 517–522 (2007)

[61] Werzer O, Cranston E D, Warr G G, Atkin R, Rutland M W. Ionic liquid nanotribology: Mica–silica interactions in ethylammonium nitrate. *Phys Chem Chem Phys* **14**(15): 5147–5152 (2012)

[62] Yokota Y, Harada T, Fukui K. Direct observation of layered structures at ionic liquid/solid interfaces by using frequency-modulation atomic force microscopy. *Chem Commun* **46**(45): 8627–8629 (2010)

[63] Sha M L, Zhang F C, Wu G Z, Fang H P, Wang C L, Chen S M, Zhang Y, Hu J. Ordering layers of [bmim][PF_6] ionic liquid on graphite surfaces: Molecular dynamics simulation. *J Chem Phys* **128**(13): 134504 (2008)

[64] Watanabe S, Nakano M, Miyake K, Tsuboi R, Sasaki S. Effect of molecular orientation angle of imidazolium ring on frictional properties of imidazolium-based ionic liquid. *Langmuir* **30**(27): 8078–8084 (2014)

[65] An R, Huang L, Long Y, Kalanyan B, Lu X, Gubbins K E. Liquid–solid nanofriction and interfacial wetting. *Langmuir* **32**(3): 743–750 (2016)

[66] Burnham N A, Colton R J, Pollock H M. Interpretation of force curves in force microscopy. *Nanotechnology* **4**(2): 64–80 (1993)

[67] Rodenbücher C, Wippermann K, Korte C. Atomic force spectroscopy on ionic liquids. *Appl Sci* **9**(11): 2207 (2019)

[68] Pethica J B, Oliver W C. Tip surface interactions in STM and AFM. *Phys Scr* **T19**: 61–66 (1987)

[69] Wang Y L, Laaksonen A. Interfacial structure and orientation of confined ionic liquids on charged quartz surfaces. *Phys Chem Chem Phys* **16**(42): 23329–23339 (2014)

[70] Steiner P, Roth R, Gnecco E, Glatzel T, Baratoff A, Meyer E. Modulation of contact resonance frequency accompanying atomic-scale stick–slip in friction force microscopy. *Nanotechnology* **20**(49): 495701 (2009)

[71] Pivnic K, Fajardo O Y, Bresme F, Kornyshev A A, Urbakh M. Mechanisms of electrotunable friction in friction force microscopy experiments with ionic liquids. *J Phys Chem C* **122**(9): 5004–5012 (2018)

[72] Sweeney J, Hausen F, Hayes R, Webber G B, Endres F, Rutland M W, Bennewitz R, Atkin R. Control of nanoscale friction on gold in an ionic liquid by a potential-dependent ionic lubricant layer. *Phys Rev Lett* **109**(15): 155502 (2012)

[73] Wang Y L, Laaksonen A, Lu Z Y. Influence of ionic liquid film thickness on ion pair distributions and orientations at graphene and vacuum interfaces. *Phys Chem Chem Phys* **15**(32): 13559–13569 (2013)

[74] Dai Z Y, You Y J, Zhu Y D, Wang S S, Zhu W, Lu X H. Atomistic insights into the layered microstructure and time-dependent stability of [BMIM][PF_6] confined within the meso-slit of carbon. *J Phys Chem B* **123**(31): 6857–6869 (2019)

[75] Romero C, Baldelli S. Sum frequency generation study of the room-temperature ionic liquids/quartz interface. *J Phys Chem B* **110**(12): 6213–6223 (2006)

[76] Fitchett B D, Conboy J C. Structure of the room-temperature ionic liquid/SiO_2 interface studied by sum-frequency vibrational spectroscopy. *J Phys Chem B* **108**(52): 20255–20262 (2004)

[77] Shim Y, Kim H J. Nanoporous carbon supercapacitors in an ionic liquid: A computer simulation study. *ACS Nano* **4**(4): 2345–2355 (2010)

Rong AN. She received her Ph.D. degree in chemical engineering from Nanjing Tech University, China, in 2013. She then worked as a postdoc researcher in Chemical and Biomolecular Engineering at North Carolina State University, USA, from 2013 to 2015. She joined Herbert Gleiter Institute of Nanoscience, Department of Materials Science and Engineering, Nanjing University of Science and Technology, China, in 2015. Her current position is an associate professor. Her research interests include the nanotribology of ionic liquids at solid interfaces, liquid–solid interfacial phenomena, gas separation, etc.

Yudi WEI. He received his B.S. degree in materials science and engineering in 2019 from Jiangsu Normal University, China. He is studying at the Department of Materials Science and Engineering, Nanjing University of Science and Technology, China, for his M.S. degree. His research interest focuses on the molecular interactions between ionic liquids and various electrode surfaces.

Xiuhua QIU. He received his B.S. degree in materials science in 2017 from Henan Polytechnic University, China. He got his M.S. degree from Herbert Gleiter Institute of Nanoscience, Department of Materials Science and Engineering, Nanjing University of Science and Technology, China, in 2021. He focused on the studies about the nanotribological behavior of ionic liquids at interfaces.

Zhongyang DAI. He received his Ph.D. degree in chemical engineering from Nanjing Tech University, China, in 2019. He joined the High Performance Computing Department in National Supercomputing Center in Shenzhen, China, in 2019. His current position is an associate researcher. His research interests include the molecular simulation for the confined systems, the prediction of molecular properties based on artificial intelligence technology, a force field development for ionic liquids based deep learning algorithm, etc.

Muqiu WU. She received her M.S. degree in materials science, Nanjing University of Science and Technology, China, in 2020. After her graduation, she joined the Herbert Gleiter Institute of Nanoscience, Nanjing University of Science and Technology, China, as a Ph.D. candidate. She is now focusing on the nanotribological behavior of confined ionic liquids.

Enrico GNECCO. He received his Ph.D. degree in physics in University of Genova, Italy, in 2001. He joined University of Basel, IMDEA Nanociencia Madrid and Friedrich Schiller University Jena, Germany, with different positions from a postdoctoral researcher up to a professor. His research focuses on atomic-scale sliding friction in different environmental conditions, scanning probe microscopy manipulation, contact mechanics, and abrasive wear processes on the nanoscale.

Faiz Ullah SHAH. He received his Ph.D. degree from the Chemistry of Interfaces, Luleå University of Technology, Sweden, in 2011. He joined the Chemistry of Interfaces, Luleå University of Technology, in 2011. His current position is an associate professor. His research area covers the synthesis of ionic liquids and the applications, e.g., batteries, lubricants, and gas separation.

Wenling ZHANG. She received her Ph.D. degree from Inha University, Republic of Korea, in 2015 and joined University of Alberta, Canada, as a postdoc (2018–2019). She is currently a professor at the School of Mechanical Engineering, Nanjing University of Science and Technology. Her research interests focus on soft matters (electro/magneto-rheological phenomena) and nanotribology (adhesion, friction, and lubrication).